

Finite element scheme based on an equivalent fluid model for the design of Micro-Perforated Panel Absorbers

Floss, Sebastian¹
Institute of Mechanics and Mechatronics
E325-3 Technical Acoustics
Getreidemarkt 9
1060 Vienna Austria

Kaltenbacher, Manfred²
Institute of Mechanics and Mechatronics
E325-3 Technical Acoustics
Getreidemarkt 9
1060 Vienna Austria

ABSTRACT

In this contribution we discuss the simulation based design and application of MPAs (micro-perforated absorbers with special emphasis on MPPs, micro-perforated plates). Thereby, we present our Finite-Element (FE) framework based on non-conforming grid techniques to allow efficient simulations of large HVAC systems. The MPPs are modeled by an homogenization ansatz using the JCAL (Johnson-Champoux-Allard-Lafarge) model based on Biot-theory. The contribution is concluded by an investigation of the behavior of MPPs under flow conditions.

Keywords: Duct, FEM, MPP

I-INCE Classification of Subject Number: 34,35,37,72,76

1. INTRODUCTION

The usage of microperforated absorbers (MPA) in HVAC systems offers some new application scenarios in case conventional materials (foams, cavity resonators) can not be used due to challenging environmental conditions, loose acoustic performance due to protection plates or demand to much design space. Especially geometrical issues (sudden cross section changes, sharp bending baffles) can have detrimental effects on pressure drop in an duct section and thus on the overall flow performance of a duct system. Already from an acoustical point of view it is beneficial to amplify e.g. the

¹sebastian.floss@tuwien.ac.at

²manfred.kaltenbacher@tuwien.ac.at

damping effect of an expansion and contraction duct section with a MPP [1] or even use a multi-layered arrangement of the plate to make the acoustic attenuation more broadband [2]. It is known that the acoustical behavior of MPAs changes under flow conditions with increasing Mach number ($Ma > 0.05$) [3]. At lower flow speeds the influence on acoustics can be neglected, it is therefore of interest to what extent a MPP can help to reduce pressure losses in a duct section. Generally, optimal MPA usage which takes into account the existing geometry or space limitations of a duct section are beyond the application range of 1-D acoustic network analogies (2-port network) [4].

Here, we propose to usage of the Finite Element Method (FEM) in combination with the JCAL (Johnson-Champoux-Allard-Lafarge, [5]) modeling ansatz of perforated screens [6]. To allow the efficient preprocessing of larger and/or more complicated HVAC structures, we suggest to mesh different parts of the absorber or duct separately and connect these individual computational regions via non-conforming grids [7].

In this work we show the application of the FEM-JCAL framework with non-conforming grids on a car muffler duct geometry. The geometrical setting and frequency range of interest are such that plane waves and higher order modes can propagate. To investigate the influence of MPPs on overall pressure drop and acoustic performance a measurement setup has been designed that can measure transmission loss (TL) and the static pressure difference between inlet and outlet of a rectangular shaped test section under flow conditions.

2. MICROPERFORATED ABSORBER

The plates that were investigated are made of metal with thicknesses of 1.6 mm and 2.6 mm aluminum and a wire mesh of about 1 mm made of stainless steel (see Figure 1). In case of a sound wave going through a perforated metal screen (more generally, a porous bulk material) one has to assume transversal wave motion in the solid metal part and a longitudinal wave motion in the air fillings [8]. General Biot-theory states that these wave motions are coupled and can be modeled accordingly. In addition, if the solid material is much more stiff than the bulk material (for a general porous material: porous air fillings plus the solid part) the solid wave motion can be neglected. Viscous and thermal effects are considered by using complex, frequency depended material parameters.

The relevant acoustic parameters are the porosity ϕ and the specific flow resistance σ . These parameters, as lists Figure 1, are fitted with a least squares algorithm by comparing absorption coefficient measurements of a single MPP in an impedance tube using the 2-microphone method [9]. The MPP was modeled as an equivalent fluid (assuming isotropic and volume averaged features, with effective density $\tilde{\rho}(\omega)$ and bulk modulus $\tilde{K}(\omega)$) [6]. The effective surface impedance was computed assuming an acoustical 2-port network with a transfer matrix $[T]$ for each section.

For a fluid and equivalent fluid the transfer matrix for the transmission of sound through a specimen of thickness h is given by

$$[T] = \begin{bmatrix} \cos(\tilde{k}h) & j\frac{\omega\tilde{\rho}}{\tilde{k}} \sin(\tilde{k}h) \\ j\frac{\tilde{k}}{\omega\tilde{\rho}} \sin(\tilde{k}h) & \cos(\tilde{k}h) \end{bmatrix}, \quad (1)$$

with \tilde{k} as the complex wave number, ω as the angular frequency.

The coupling of MPP section (thickness h) and air cavity section (length D), as displayed


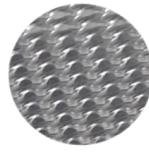

Parameters	MPP (1.6 mm)	MPP (2.6 mm)	wire mesh (1 mm)
			
σ/Nsm^{-4}	502100	309400	230800
ϕ	0.048	0.089	0.152

Figure 1: Panel materials under investigations; specific flow resistance σ and porosity ϕ

in Figure 2, is achieved by

$$[\mathbf{T}]_{1,2} = \prod_{n=1} [\mathbf{T}]_{n,n+1}. \quad (2)$$

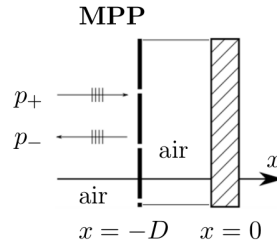


Figure 2: Microperforated absorber configuration; micro-perforated plate in front of air cavity of certain length D ; forward propagating pressure wave p_+ , reflected pressure wave p_- .

3. MEASUREMENT TECHNIQUES

To evaluate the acoustic performance of different MPP designs we measure the transmission of sound through a test section. The pressure drop is investigated via static pressure drop measurements under stationary volume flow rate, determined by a Venturi probe section.

3.3.1. Acoustic Transmission Loss

If one can determine the sound pressure and particle velocity in front and after a test section, one can calculate absorption, reflection and transmission within that section. This is achieved by using the transfer matrix method [10]. It is necessary to conduct two measurements with different end pieces (index $j=1,2$).

The transfer matrix $[\mathbf{T}]$ computes by

$$[\mathbf{T}] = \begin{bmatrix} p_{a,1} & p_{a,2} \\ v_{a,1} & v_{a,2} \end{bmatrix}_{x=0}^{-1} \begin{bmatrix} p_{a,1} & p_{a,2} \\ v_{a,1} & v_{a,2} \end{bmatrix}_{x=h} \quad (3)$$

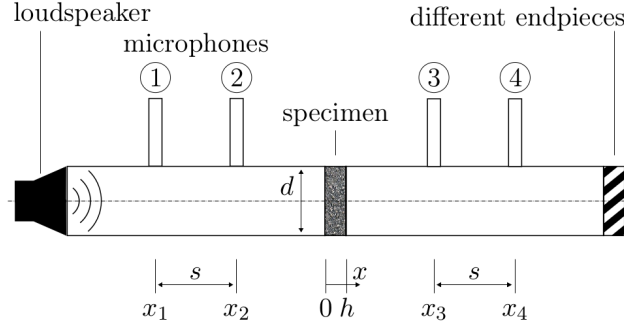


Figure 3: Impedance tube with 4 microphones, specimen thickness h , microphone distance s , impedance tube diameter d

with sound pressure and particle velocity in front ($x = 0$) and after ($x = h$) the test section, respectively specimen. The transmission loss (TL) is then calculated with

$$TL = 20 \log_{10} \left(\frac{p_a(0)}{p_a(h)} \right). \quad (4)$$

The measurement principle is based on the assumption that only plane waves can propagate in the microphone measurement segment. This is only the case if higher order modes are sufficiently damped out in front of the microphone segments. The high frequency limit (cut-on frequency) f_u [9] can be estimated by

$$f_u = 0.58 \frac{c}{d}, \quad f_u = 0.5 \frac{c}{h} \quad (5)$$

for circular cross sections (d), quadratic cross sections (h) and c as the speed of sound. There is also a limit to avoid geometrical aliasing, which gives a formula for the microphone distance s [9]:

$$f_u = 0.45 \frac{c}{s} \quad (6)$$

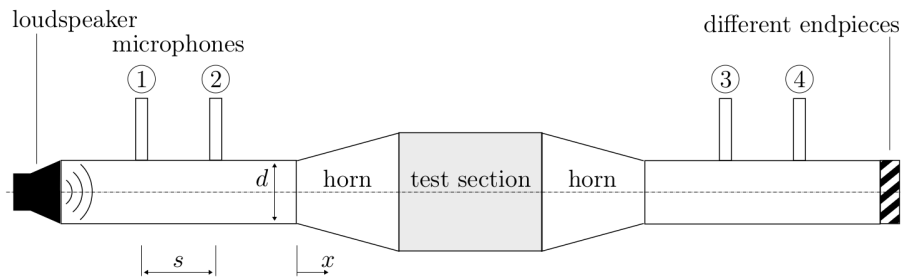


Figure 4: Impedance tube with 4 microphones and horns for smooth impedance transition

The chosen dimensions of $d=29$ mm for the circular measurement cross section, $h=25$ mm for the quadratic cross section and microphone distance $s=20$ mm allow for a measurement range from 200 Hz to 6400 Hz.

The test sections on the other hand need to have arbitrary shapes, so higher order modes can propagate there. With the help of 3D printed horn adapters, the test section geometry is connected to the microphone segment cross section shape (see Figure 4). The horns have an exponential spline shape, so that a continuous impedance transition reduces reflections and thus damping in the horn region in the frequency range up to 1000 Hz.

3.3.2. Pressure drop

To measure the pressure drop between point P1 and P2 (see Figure 5) of the test section, two additional sections (section P1 and P2 in Figure 6) were added for measuring the static pressure below the viscous boundary layer on the circumference of the duct in front and after the test section. Four pressure holes (see Figure 6) on each measurement section are hydraulically coupled and the so averaged pressure fluctuations on P1 and P2 are detected by a differential pressure sensor. The same principle is used in the venturi segment (Figure 5) to be able to calculate the flow rate from the differential pressure drop induced by the venturi profile. The Venturi flow meter was checked with different defined flow rates from a commercial flow rate generator (Thermojet Environment Simulator [11]). The acoustic absorbers were tested under three different flow rates which resulted in air speeds of 5 m/s, 10 m/s and 12.5 m/s in the measurement segment. This, of course, results in lower velocity above the absorber.

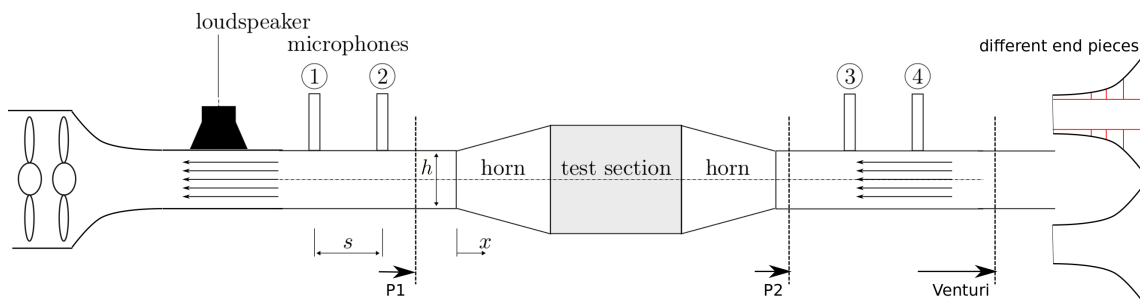


Figure 5: Quadratic cross section impedance duct with 4 microphones, horns for smoother impedance transition, microphone distance s and measurement points for static pressure and flow rate (Venturi)

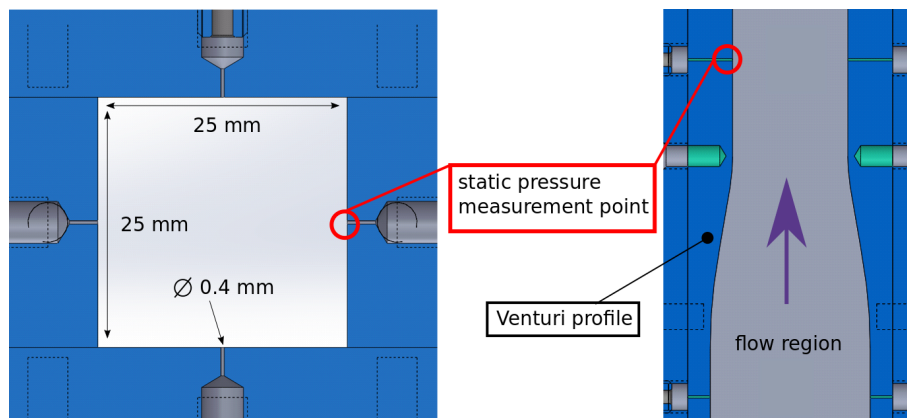


Figure 6: Magnification and detailed view of section P1, P2 and Venturi section for flow rate measurement

The flow rates were generated by two axial fans. The air would then pass the absorber in grazing incident in a 25 mm x 86 mm channel (see Figure 7). To be able to measure the acoustic wave entering and interacting with the absorber under flow conditions, the microphones in Figure 5 were recessed from the inner surface of the duct by 1.5 cm and the cavity was covered by a perforated screen. The recessed microphone positioning plus the covering will manifest itself in a higher transmission loss that has to be taken into account when analyzing the measured data.

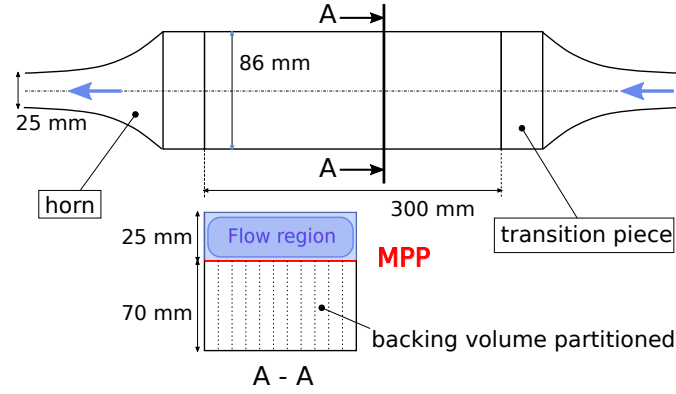


Figure 7: Detailed view of the test section with horn segments for smooth impedance transitioning and flow guiding; cross cut to show dimensions and flow region

4. SIMULATION

While the proposed measurement setup enables the acoustic testing of new absorber designs, the usage of the non-conforming grid technique allows for the efficient simulation of more complicated absorber structures. In the FE simulation we seek a solution for the acoustic pressure p_a fulfilling the following partial differential Equation 7 (inhomogeneous Helmholtz equation).

$$\frac{\omega^2}{\tilde{K}} p_a + \nabla \cdot \left(\frac{1}{\tilde{\rho}} \nabla p_a \right) = 0, \quad (7)$$

In Equation 7 ω denotes the angular frequency, $\tilde{\rho}$ the effective fluid density and \tilde{K} the effective bulk modulus. In the air region, the effective material parameters take on the values of ρ_0 and K_0 in air.

4.4.1. Modeling

Johnson-Champoux-Allard-Lafarge (JCAL, [8]) This model is based on the governing equations for single pores. The pores can be tubes or have a changing cross section. There exist analytical solutions for the high and low frequency limits, but for the domain in between the governing equations are adapted to fit empirical data (a semi-empirical model, in comparison to e.g. Delany-Bazely-Miki model which is purely empirical).

The effective values derive from six physical values. Beside the static flow resistance and porosity these are [8]:

Tortuosity in the high frequency limit α_∞ It states how strong the orientation of the pores deviates from a right angle. The effective density in the high frequency limit is $\tilde{\rho} = \alpha_\infty \rho_0$.

Viscose charakteristic length Λ Corresponds to the thickness of the viscous boundary layer in the pores.

Thermal charakteristic length Λ' Corresponds to the ratio of pore volume to pore surface.

Static thermal permeability k'_0 Describes the ratio of mean temperature to the time derivative of the pressure, but has no direct physical meaning.

Effective density and bulk modulus are therefore calculated from

$$\tilde{\rho}(\omega) = \frac{\alpha_{\infty}\rho_0}{\phi} \left[1 + \frac{\sigma\phi}{j\omega\rho_0\alpha_{\infty}} \sqrt{1 + j\frac{4\alpha_{\infty}^2\mu\rho_0\omega}{\sigma^2\Lambda^2\phi^2}} \right], \quad (8)$$

$$\tilde{K}(\omega) = \frac{\gamma p_0/\phi}{\gamma - (\gamma - 1) \left[1 - j\frac{\phi\kappa}{k'_0 C_p \rho_0 \omega} \sqrt{1 + j\frac{4k'_0{}^2 C_p \rho_0 \omega}{\kappa\Lambda^2\phi^2}} \right]^{-1}}. \quad (9)$$

There are some constant values contained which depend on the thermodynamic conditions of air (we assume standard conditions). These are the dynamic viscosity $\mu = 18.232 \cdot 10^{-6}$ Pas, isentropic exponent $\gamma = 1.4$, thermal conductivity $\kappa = 25.684 \cdot 10^{-3}$ W/(m K) and specific heat of air under constant static pressure $C_p = 1.006825 \cdot 10^3$ J/(kg K).

4.4.2. Non-conforming grids

The non-conforming grid technique allows for an individual mesh generation of each subdomain. At the interfaces the physical transmission conditions are fulfilled by the enhanced FE formulation [7]. Figure 8 demonstrates the advantages in performing the preprocessing.

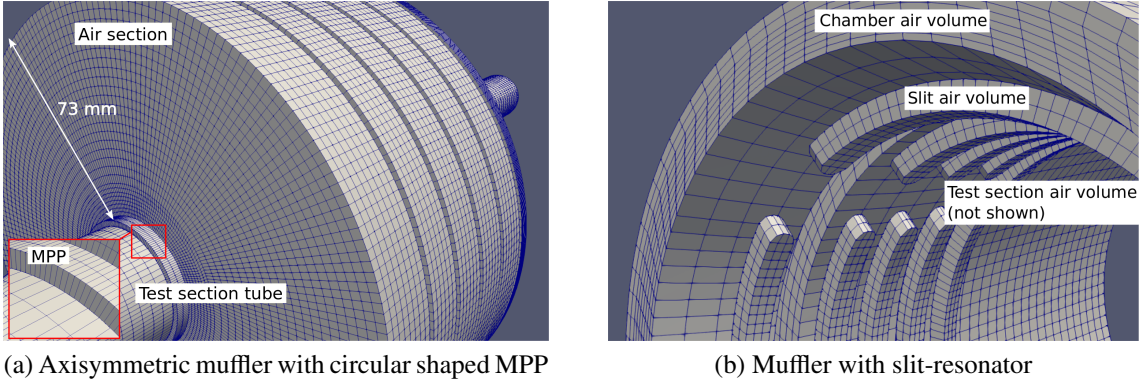


Figure 8: Two simulation grids with non-conforming grids at joint part interfaces

The transmission loss was computed from numerical data at microphone positions 1, 2 and 3 in Figure 4. Additionally, the FE framework allows to create a non-reflecting end piece by using the a perfectly matched layer (PML). Therefore the computational effort can be reduced by applying the 3-microphone transfer matrix method [12]).

5. RESULTS

In this part the results from non-conforming grid simulations and transmission loss measurements of car muffler are shown. This section is concluded by static pressure drop and transmission loss measurements of a rectangular shaped duct silencer part.

5.5.1. Muffler

By comparing the simulation results in Figure 9 and Figure 10 one can first see that the transition of the duct geometry with the horns produces an increase in transmission

loss up to 1500 Hz. But in the simulation this effect becomes weaker when reaching the higher frequency regime.

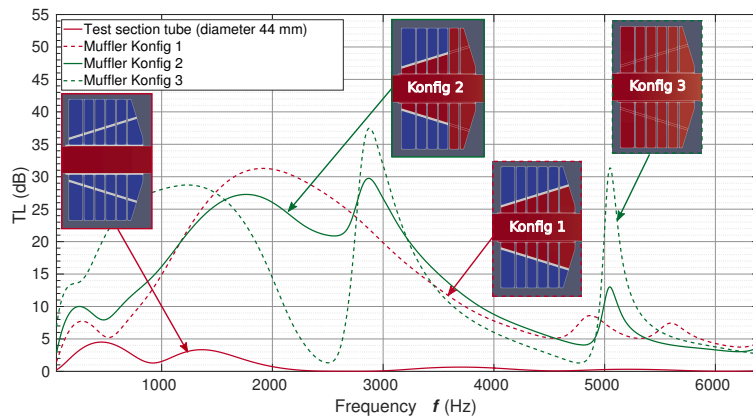


Figure 9: Simulated transmission loss (TL) of different muffler designs

When different sections of the muffler are added the whole design becomes more locally reacting and behaves like a single MPP in front of a sound hard backing wall. This offers a solution for the phenomenon that a single circular MPP has high damping effect up to 3000 Hz, but then the damping effect drops to a almost constant 5 dB transmission loss in the higher frequency region. By adding more cavity like structures of different lengths one could achieve a higher transmission loss beyond 3000 Hz.

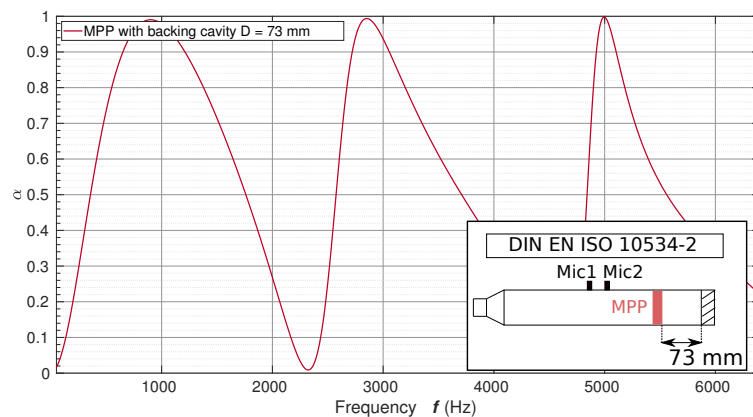


Figure 10: Simulation result of the absorption coefficient of a single 1.6 mm MPP in front of a backing cavity of length $D = 73$ mm, simulated according to ISO standard EN 10534-2

The simulation and measurement of the transmission loss of the slit resonator (Figure 11) show good agreement up to 5000 Hz. Since the cut-off frequency of the 44 mm tube section is roughly 4500 Hz, one might see an effect of the higher order mode propagation here. Also the final 3D printed horn design joints to the slit resonator might not represent a smooth enough impedance jump which is on the other hand fully accounted for in the simulation and therefore an additional transmission loss is generated in the measurements.

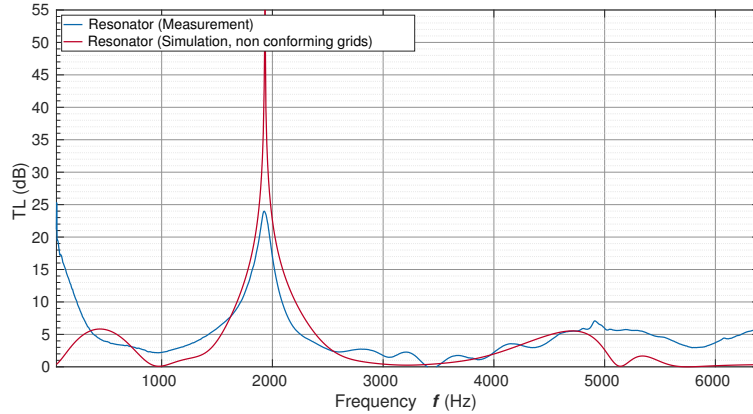


Figure 11: Measured and simulated transmission loss of a slit resonator design without MPPs

5.5.2. Rectangular chamber silencer

The rectangular chamber silencer segment should mimic the situation when flow and acoustic waves impinge on the absorber in a grazing incident. From an acoustic point of view this is not an optimal scenario, but allows to study a more challenging design. For brevity Figure 12 only shows the case of the partitioned back volume of length 70 mm covered by a 1.6 mm MPP, 2.6 mm MPP and the 1.0 mm thick wire mesh. The reference measurement is the transmission loss of the 25 mm quadratic channel only. The reference transmission loss up to 4500 Hz is due to the fact the microphones 1 to 4 in Figure 5 were recessed to measure less hydrodynamic pressure fluctuations in additional measurements runs when acoustic is to be measured under flow conditions. The cavity was also covered by a wire mesh which accounts for the reference losses from 4500 to 6400 Hz. By comparing again Figure 10 one can see that the back partitioning attenuates the single layer MPP behavior. The wire mesh shows the highest acoustic damping capabilities.

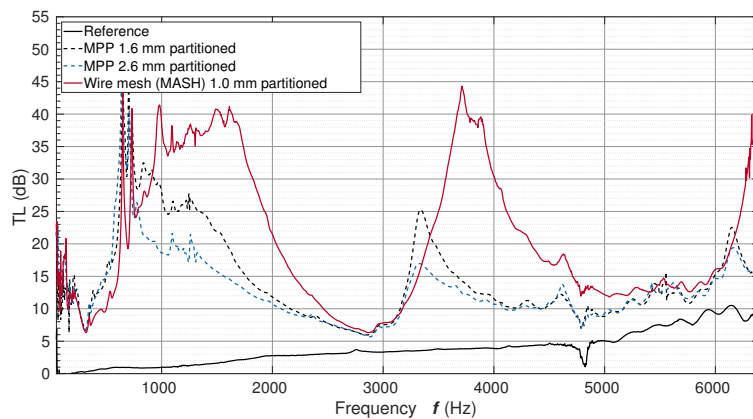


Figure 12: Measured transmission loss of three different MPPs covering a partitioned back volume; reference measurement show losses due to recessed microphone positions and covering wire mesh

As can be seen from Table 1, the MPP is capable of guiding the fluid flow. For brevity, only the MPP with 2.6 mm thickness and the wire mesh are shown here, but one must state that the higher the flow velocity the less effective are the MPPs from an hydrodynamic

point of view. Although the wire mesh has the the highest acoustic damping effects, it is much less effective in guiding the flow than the 2.6 mm MPP. From a design point of view, there seems to be a trade-off between acoustic and hydrodynamic performance of these novel MPA application scenarios even at lower flow speeds. Again it is emphasized that the flow speeds in test section are smaller than in the venturi measurement segment when impinging on the absorber. This on the other hand shows how critical the guiding of the flow can become. In the expanding horn shape the flow structures at the inlet domain of the test section, due to their suspected only slightly turbulent nature at lower flow speed (only induced due to sudden geometry changes), already seem to be more sensitive to a guiding structure. The values in the table show the mean values of flow speed and pressure drop with standard deviation.

Flow values $\bar{x} \pm s$	Alu plate	no plate	MPP (2.6 mm)	wire mesh (1 mm)
Flow speed /ms ⁻¹	$\Delta P / Pa$	$\Delta P / Pa$	$\Delta P / Pa$	$\Delta P / Pa$
range 5	14.7 ± 1.8 5.5 ± 0.21	17.9 ± 1.7 5.0 ± 0.28	13.4 ± 1.5 5.0 ± 0.23	14.6 ± 1.7 4.9 ± 0.24
range 10	43.5 ± 3.6 9.9 ± 0.15	65.1 ± 4.1 10.1 ± 0.17	49.7 ± 3.6 10.0 ± 0.13	56.8 ± 3.7 10.0 ± 0.14
range 12.5	73.2 ± 7.1 12.9 ± 0.11	96.7 ± 7.5 12.5 ± 0.14	79.4 ± 6.7 12.6 ± 0.1	84.0 ± 5.6 12.1 ± 0.13

Table 1: Mean values and standard deviation of flow speed in the venturi measurement segment and pressure drop within the test section; comparing full Aluminum and MPP plate with no plate guiding the flow

6. CONCLUSIONS

Transmission loss and pressure drop measurement techniques for the characterization of more complicated micro-perforated panel designs have been shown. The FEM framework makes use of non-conforming grids and MPP modeling according to the JCAL approach. The comparison of measurements and FEM simulations of different silencer designs show good agreement. By evaluating the pressure drop of a silencer test section in a grazing flow scenario, it could be shown that a MPP can guide the flow, but as the flow velocities increase, this effect appears to loose its effectiveness. Further investigations of this benchmark suited test setup will follow, including higher flow velocities and more complicated structures like baffles. Also the measurement of transmission loss under flow conditions and the incorporation of flow effects in the JCAL-non-conforming-grid framework is of interest.

7. REFERENCES

- [1] D. Y. Maa. Potential of micro-perforated panel absorbers. *Journal of the Acoustical Society of America*, 104(5):2861–2866, 1998.
- [2] S. Floss, M. Kaltenbacher, and G. Karlowatz. Application and simulation of micro-perforated panels in hvac systems. *SAE Technical Paper*, 2018.
- [3] M. Abom and S. Allam. A new type of muffler based on microperforated tubes. *Journal of Vibration and Acoustics*, 133:031005–1–031005–6, 2011.
- [4] M. Heckl and H.A. Müller. *Taschenbuch der technischen Akustik*. Springer Verlag, Berlin, 1994.
- [5] J.-F. Allard and Y. Champoux. New empirical equations for sound absorption in rigid frame porous media. *Journal of the Acoustical Society of America*, 91(6):3346–3353, 1992.
- [6] L. Jaouen and F.-X. Bécot. Acoustical characterization of perforated facings. *Journal of the Acoustical Society of America*, 129(3):1400–1406, 2011.
- [7] M. Kaltenbacher and S. Floss. Nonconforming finite elements based on nitsche-type mortaring for inhomogeneous wave equation. *Journal of Theoretical and Computational Acoustics*, page 1850028, June 2018.
- [8] Jean F. Allard and Noureddine Atalla. *Propagation of Sound in Porous Media*. John Wiley & Sons, 2009.
- [9] ISO 10534-2. Akustik – bestimmung des schallabsorptionsgrades und der impedanz in impedanzrohren teil 2: Verfahren mit Übertragungsfunktion, 2001. Norm.
- [10] ASTM E2611. Standard test method for normal incidence determination of porous material acoustical properties based on the transfer matrix method, 2006. Normentwurf.
- [11] Thermojet ES Precision Temperature Cycling System. https://www.spscientific.com/Products/Thermal_Products/FTS_Systems/Air_Stream/ThermoJet_ES_Precision_Temperature_Cycling_System/. Accessed: 2019-02-24.
- [12] Ralph T. Muehleisen and C. Walter Beamer. Comparison of errors in the three- and four-microphone methods used in the measurement of the acoustic properties of porous materials. *Acoustics Research Letters Online*, 3(4):112–117, 2002.
- [13] CFS Userguide. https://cfs-doc.mdm.tuwien.ac.at/mediawiki/index.php/Main_Page. Accessed: 2019-02-24.
- [14] F. Egner. *Acoustic Characterization of Air Ducts*. Technical University of Vienna. Master Thesis, Vienna, 2018.